Research Article | Open Access

Microstructures

Zhang et al. Microstructures 2026, 6, 20260127 DOI:10.20517/microstructures.2026.79

High-performance aqueous zinc-ion batteries with highly oriented MFI zeolite nanosheet separators

Haoyu Zhang[1], Sirui Chen[1], Huang Lin[1], Anding Xu[1], Xin Wen[1], Longtao Ma[2], Yu Han[1,3,4], Hui Zhang[1,3,4]

Keywords:
Aqueous zinc-ion batteries, nanoporous, zeolite nanosheets, inorganic separator

Citation: Zhang, H.; Chen, S.; Lin, H.; Xu, A.; Wen, X.; Ma, L.; Han, Y.; Zhang, H. High-performance aqueous zinc-ion batteries with highly oriented MFI zeolite nanosheet separators. *Microstructures* **2026**, *6*, 20260127. https://dx.doi.org/10.20517/microstructures.2026.79

Received: 23 Apr 2026
First Decision: 17 Jun 2026
Revised: 21 Aug 2026
Accepted: 25 Aug 2026
Published: 24 Sep 2026

Academic Editor: Yida Deng
Copy Editor: Fangling Lan
Production Editor: Fangling Lan

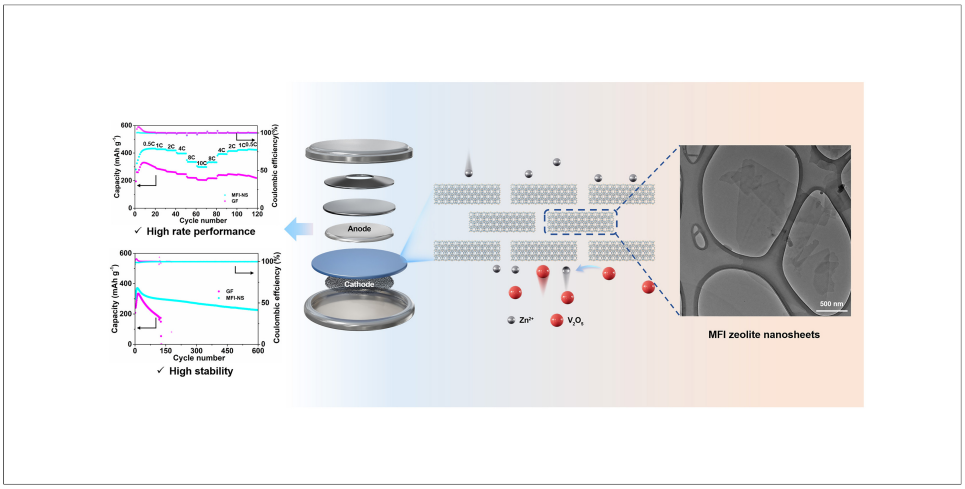

Abstract

Aqueous zinc-ion batteries (AZIBs) offer intrinsic safety and cost advantages for grid-scale energy storage, yet their practical deployment is severely hindered by parasitic hydrogen evolution and uncontrollable dendrite growth. Zeolite-based separators have emerged as a promising solution; however, conventional designs rely on randomly oriented zeolites and polymer binders, which compromise ion transport efficiency and mechanical robustness. Here, we demonstrate that binder-free separators fabricated from highly [010]-oriented MFI zeolite nanosheets (MFI-NS) can overcome these limitations. The binder-free strategy endows the MFI-NS separator with a tensile strength two orders of magnitude higher than that of commercial glass-fiber (GF) separators, providing exceptional mechanical robustness against dendrite penetration. The self-assembled lamellar stack of MFI-NS ensures straight channels well-aligned perpendicular to the electrode surface, delivering a Zn^{2+} transference number 266% higher and an ionic conductivity 62% higher than those of separators comprising randomly oriented MFI particles, thereby enabling rapid and

[1]School of Emergent Soft Matter, Guangdong Provincial Key Laboratory of Functional and Intelligent Hybrid Materials and Devices, South China University of Technology, Guangzhou 510640, Guangdong, China.
[2]School of Materials Science and Engineering, Guangdong Provincial Key Laboratory of Advanced Energy Storage Materials, South China University of Technology, Guangzhou 510641, Guangdong, China.
[3]Center for Electron Microscopy, South China University of Technology, Guangzhou 511442, Guangdong, China.
[4]State Key Laboratory of Pulp and Paper Engineering, South China University of Technology, Guangzhou 510640, Guangdong, China.

Correspondence to: Dr. Hui Zhang, School of Emergent Soft Matter, Guangdong Provincial Key Laboratory of Functional and Intelligent Hybrid Materials and Devices, South China University of Technology, Guangzhou 510640, Guangdong, China; Center for Electron Microscopy, South China University of Technology, Guangzhou 511442, Guangdong, China; State Key Laboratory of Pulp and Paper Engineering, South China University of Technology, Guangzhou 510640, Guangdong, China. E-mail: huizhang2023@scut.edu.cn

efficient Zn^{2+} transport. Concurrently, the uniform micropores in MFI-NS effectively suppress hydrogen evolution and retard dendrite formation. These synergistic benefits markedly enhance the electrochemical performance of AZIBs. The V_2O_5||MFI-NS||Zn full cell delivers a high specific capacity of 420 mAh g^{-1} at 1 A g^{-1} and retains 71% of its initial capacity after 1,200 cycles, which substantially outperforms the cells with separators comprising conventional GF or randomly oriented MFI particles. This work establishes crystallographic orientation engineering in zeolite separators as a powerful strategy for addressing multiple degradation mechanisms in AZIBs.

INTRODUCTION

The rapid integration of renewable energy, driven by the urgent need to address climate change and further intensified by the escalating power demands of artificial intelligence, has made the development of grid-scale energy storage systems a critical technological priority[1,2]. Consequently, secondary batteries suitable for large-scale applications have garnered increasing attention[3-5]. After decades of innovation, aqueous zinc-ion batteries (AZIBs) have emerged as a particularly promising candidate, offering a compelling combination of intrinsic safety, economic viability, and high capacity (820 mAh g^{-1})[6,7]. Nevertheless, the reliable deployment of AZIBs faces challenges posed by detrimental dendrite propagation[8,9], parasitic hydrogen/oxygen evolution[9-11], dissolution of active materials[12], and corrosion and passivation of electrodes[13-15], which critically undermine the cycling stability and necessitate the coordinated innovations of electrodes[16-20], electrolytes[21-23] and separators[24-26]. Compared to optimizing single electrochemical components, engineering the separator is capable of addressing those intertwined issues, given its central role in mediating the interactions between electrolytes and electrodes[27].

Nanoporous materials such as metal-organic frameworks[28-30], covalent-organic frameworks[31], and zeolites[32-34] offer highly tunable porosity at the nanometric scale, which presents significant potential for regulating the transportation of ions and water molecules, and thus have recently been explored as promising candidates for separators in high-performance AZIBs. Among these, zeolites are particularly notable for their chemical stability, cost-efficiency, and industrial scalability.

Compared to conventional glass-fiber (GF) separators, the zeolite-based membranes can markedly improve the performance across a wide range of current densities, as evidenced by enhanced capacity retention during cycling and superior rate behavior[35-37]. These performance enhancements arise from several key factors. The ordered micropores in the crystallites facilitate the homogeneous deposition of Zn^{2+} ions on the anode, effectively mitigating the detrimental growth of dendrites[37]. Concurrently, the inherent water-adsorption capability and size-exclusion properties of these micropores minimize parasitic side reactions at the anode interface[35,37]. Furthermore, the micropores physically block the shuttling of soluble species generated at the cathode[32,38,39], such as V^{3+}/VO^{x+}[32,40] or I_3^-[36], which suppresses cathode dissolution[41], alleviates anode erosion[42], and mitigates self-discharge[32]. Notably, these advantages are not limited to their use as bulk separators. Similar protective effects have been achieved by filling zeolites into the large pores in GF separators[42] or by coating zeolites directly onto zinc anodes[41]. This versatility further underscores the potential of zeolites to enhance the longevity and reliability of AZIBs.

Zeolites with different topological structures and pore sizes have different application scenarios. In the context of AZIB separators, Zhu and coworkers systematically evaluated nine zeolites and identified an optimal pore size window of 5-7 Å. Within this range, ZSM-5 and beta zeolites demonstrate superior specific capacity and capacity retention over 2,000 cycles[35]. The transport of guest molecules and ions through zeolite crystals is critically influenced by the diffusion path length along the primary channels[43]. For optimal performance, the diffusion pathway should generally be minimized, and the crystallographic orientation should be well-aligned to maximize mass transport efficiency. These structural requirements can be fulfilled

by assembling ultrathin nanosheets prepared by bottom-up synthesis[44,45]. While this approach is well-established for ZSM-5, it remains challenging for beta zeolites. Thus, the present work primarily focuses on the former.

ZSM-5 has a topology of MFI and is probably the most extensively utilized zeolite. With dC5 as the structural direct agent, Jeon *et al.*[44] synthesized 5 nm thick nanosheets. Since then, considerable efforts have been directed towards fabricating large-area membranes via coating and secondary growth methods[46,47]. Such membranes have demonstrated marked advantages over conventional zeolite membranes in the separation of xylene and butane isomers[46,48,49]. More recently, separators based on MFI nanosheets (MFI-NS) have been used for flow batteries[39,40,50,51] and lithium-ion batteries[52,53]. In these systems, the well-aligned straight channels within the membrane are unequivocally confirmed to enhance charge-carrier transport relative to traditional zeolite membranes[39,40,52]. However, previous efforts to integrate MFI-NS into battery systems have heavily relied on polymer binders or matrices, which inherently compromise the intrinsic ion-transport and mechanical properties of zeolites.

In this work, we exploit the self-assembly capability of MFI-NS to fabricate binder-free separators with well-aligned straight channels for AZIBs. It is demonstrated that this strategy effectively suppresses dendrite growth and mitigates parasitic side reactions, substantially extending the cycling life of AZIBs. Specifically, the V_2O_5||MFI-NS||Zn full cell delivers a specific capacity of 420 mAh g^{-1} at a current density of 1 A g^{-1} and retains 71% of its initial capacity after 1,200 cycles, demonstrating exceptional cycling stability. These merits underscore the strong potential of MFI-NS for improving the safety and service life of next-generation AZIBs.

EXPERIMENT AND METHOD

Synthesis of MFI-NS

MFI-NS were synthesized following the method reported by Jeon *et al.*[44], which relies on the preparation of the structure-directing agent (SDA), dC5. To obtain high-quality dC5, 18.90 g of 1,5-diaminopentane and 82.35 g of potassium carbonate were added to 450 mL of 2-butanone in a two-neck round-bottom flask. Under vigorous stirring (1,400 rpm), the mixture was slowly heated to 80 °C under an argon atmosphere, followed by dropwise addition of 108 mL of 1-iodopropane. The reaction was maintained under reflux for 12 h in the absence of light to prevent side reactions. After cooling, the reaction mixture was filtered to remove potassium salts, and the filtrate was concentrated by rotary evaporation to remove 2-butanone.

To further purify the product, the obtained solids were redissolved in 250 mL of 2-butanone, and stirred at 1,400 rpm for 1 h. Subsequently, an equal volume of ethyl acetate was added, and the mixture was further stirred at 1,400 rpm for an additional 12 h. Rotary evaporation was again employed to recover the solids from the filtrate; this purification cycle was repeated four times. Residual KI remained as a trace impurity, which was subsequently removed by dissolving the solids in dichloromethane, followed by filtration. The resulting filtrate was concentrated by rotary evaporation to obtain pure dC5.

For the synthesis of MFI-NS, 0.2406 g of dC5 was added to a KOH solution (0.1120 g KOH in 17.97 mL deionized water) contained in a 100 mL polytetrafluoroethylene (PTFE) beaker. The mixture was stirred until complete dissolution, after which 1.85 mL of tetraethyl orthosilicate was introduced and stirred continuously for 16 h under ambient conditions. The sol was then filtered through a 0.45 μm polypropylene membrane to remove insoluble residues. The filtrate was transferred into a 50 mL PTFE autoclave liner, to which MFI-type zeolite seed crystals were added and dispersed by shaking. The autoclave was sealed and heated for 4 days at 140 °C. The resulting MFI-NS were collected by centrifugation and washed repeatedly with deionized water until the supernatant reached a neutral pH.

Commercial ZSM-5 zeolites with randomly oriented granular particles (Tianjin Yuanli Chemical Co., Ltd.) were used as a reference to evaluate the effect of well-aligned straight channels.

Preparation of MFI-NS separators

MFI-NS separators were prepared by vacuum filtration of a well-dispersed MFI-NS suspension in ethanol. During filtration, the suspension was intermittently stirred to maintain uniform dispersion of the nanosheets. After filtration and drying, the resulting MFI-NS membrane was carefully peeled from the filter and cut to the desired shape. The typical areal mass loading is approximately 14.1 mg cm^{-2}. The membrane was then calcined in a muffle furnace at 550 °C for 6 h with a heating rate of 2 °C min^{-1}.

Fabrication of cathode

Commercial V_2O_5 powder was treated according to the method described in Ref.[35]. Briefly, 0.6000 g of V_2O_5, 1.4820 g of oxalic acid, and 15 mL of deionized water were mixed and stirred until complete dissolution. The resulting solution was dried in a vacuum oven at 70 °C to remove the solvent, and the obtained powder was calcined in a muffle furnace at 400 °C for 2 h. After cooling to room temperature, the product was ground for 30 min to obtain the treated V_2O_5 powder.

To fabricate the cathode, the treated V_2O_5, carbon black, and polyvinylidene fluoride were mixed at a mass ratio of 7:2:1. Subsequently, a suitable amount of N-methyl-2-pyrrolidone (NMP) was added, and the mixture was thoroughly ground for 1 h to form a homogeneous slurry. The slurry was then uniformly coated onto a 30-μm-thick titanium foil and dried at 80 °C to obtain the final V_2O_5 electrode, allowing NMP to completely evaporate. The mass loading was approximately 0.7 mg cm^{-2}.

Electrochemical characterizations

Coin cells were assembled with the following stacking order: V_2O_5 cathode, separator (soaked in 3 M $ZnSO_4$), zinc anode, gasket, and spring sheet. Zn||Zn symmetric cells and Zn||Cu half-cells were assembled following the same procedure. All assembled cells were allowed to rest for 12 h before electrochemical testing. Cyclic voltammetry (CV), Tafel polarization and linear sweep voltammetry were performed on an electrochemical workstation (CHI 440E, Chenhua, China). Electrochemical impedance spectroscopy (EIS) and chronoamperometry (CA) were examined on a separate electrochemical workstation (Squidstat Plus, Admiral, USA). The ionic conductivity was calculated by $\frac{L}{S \cdot R}$, where L, S, and R are the separator thickness, the contact area, and the resistance, respectively. The Zn^{2+} transference number was evaluated by $\frac{I_S(\Delta V - I_0 R_0)}{I_0(\Delta V - I_S R_S)}$, where ΔV, I_0, R_0, I_s and R_s are potential, initial current, initial resistance, steady-state current and steady-state resistance, respectively. Galvanostatic charge-discharge tests were carried out using a Neware battery testing system.

Structural, spectroscopic and mechanical characterizations

Morphological images were acquired using a scanning electron microscope (Quattro, Thermo Fisher, USA). X-ray diffraction (SmartLab, Rigaku, Japan) patterns were recorded on an X-ray diffractometer with Cu Kα irradiation. Nitrogen adsorption-desorption isotherms were measured at liquid nitrogen temperature using a surface area analyzer (3Flex, Micromeritics, USA). All samples were evacuated at 120 °C under vacuum overnight before measurements. Transmission electron microscopy (TEM) images and selected area electron diffraction (SAED) patterns were collected on a transmission electron microscope working at 200 kV (Talos F200X, Thermo Fisher, USA).

Fourier-transform infrared (FT-IR) spectra were recorded using a spectrometer (FT/IR-4X, JASCO, Japan) working under ambient conditions. Tensile tests were performed on a micro-mechanical testing machine (MESOTS-200N, Nanjing Ruize, China) with a displacement rate of 0.2 mm min^{-1}.

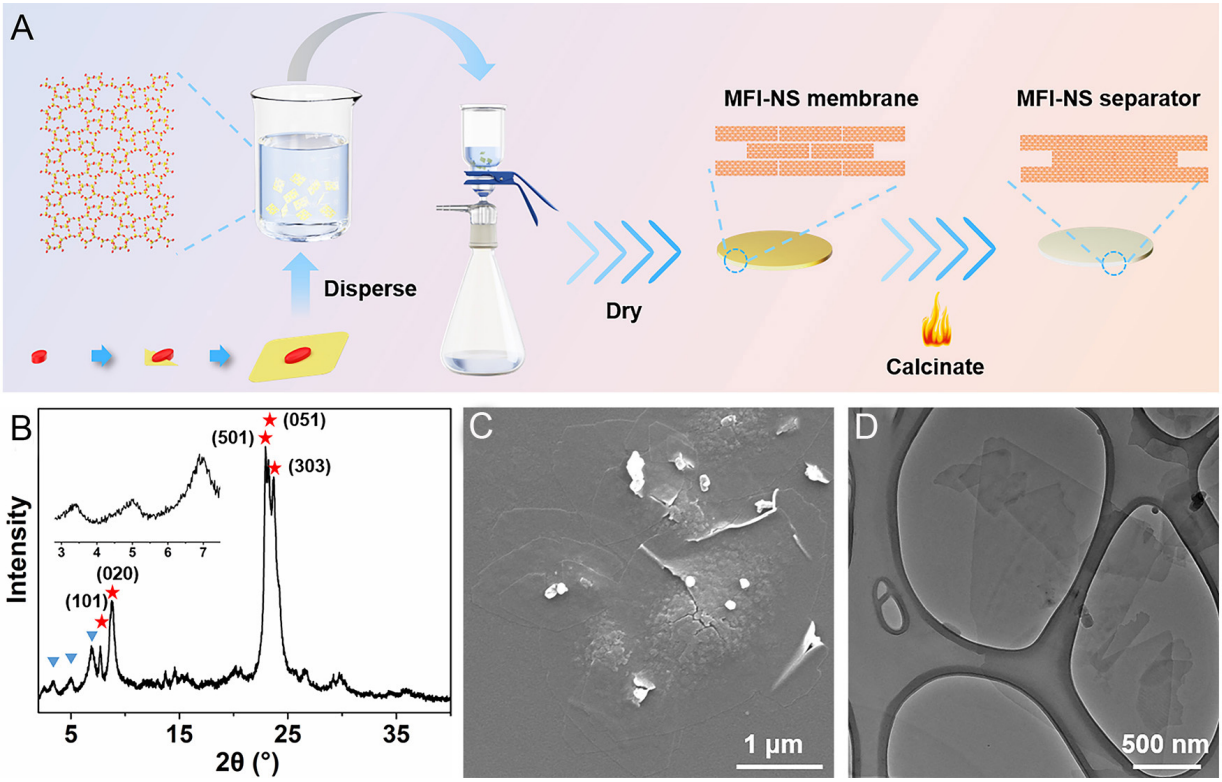

Figure 1. (A) Schematic illustration of the fabrication process of the MFI-NS separator. (B) XRD diffraction pattern of MFI-NS. Five strong peaks are labeled. Three additional weak peaks beyond the typical ZSM-5 diffractions are highlighted by blue triangles and enlarged in the inset. (C) SEM and (D) TEM images of MFI-NS.

RESULTS AND DISCUSSION

Novel MFI-NS separators with highly oriented straight channels were fabricated following the procedure illustrated in Figure 1A. Briefly, MFI-NS with high aspect ratios were first synthesized via a bottom-up approach. The MFI-NS membrane was then prepared by vacuum filtration, followed by calcination to remove the SDA and promote inter-nanosheet condensation.

The XRD pattern of the as-synthesized MFI-NS displays the characteristic diffraction peaks of ZSM-5, such as the (101), (020), (501), (051), and (303) reflections[39]. Beyond these typical features, three additional low-angle reflections below 8° are observed, which can be ascribed to the formation of a superlattice structure resulting from interactions among template molecules[54]. In bulky ZSM-5, the intensity of (020) reflection is generally lower than that of (101) reflection. The markedly reversed relative intensity in Figure 1B suggests a preferential orientation of [010]. Consistent with previous reports[44], the nanosheets consist of 50-100 nm thick small cores and ~5 nm thick peripheral regions that laterally extend 1-3 μm [Figure 1C and D, Supplementary Figure 1]. The SAED pattern of MFI-NS is unambiguously indexed with the [010] zone-axis reflections of ZSM-5 [Supplementary Figure 2], indicating that the longitudinal direction of the nanosheets aligns with the *b*-axis, which agrees well with the XRD pattern.

The MFI-NS membrane was prepared by vacuum filtration, which results in the lamellar stacking of nanosheets [Supplementary Figure 3A]. The thickness of the membrane is readily controlled by adjusting the concentration of the MFI-NS suspension [Supplementary Figure 3B-D]. To balance mechanical robustness and cost, a membrane of approximately 0.14 mm in thickness was selected for microstructural and electrochemical characterizations. In the as-assembled membrane, the SDA occupies the micropores, leaving

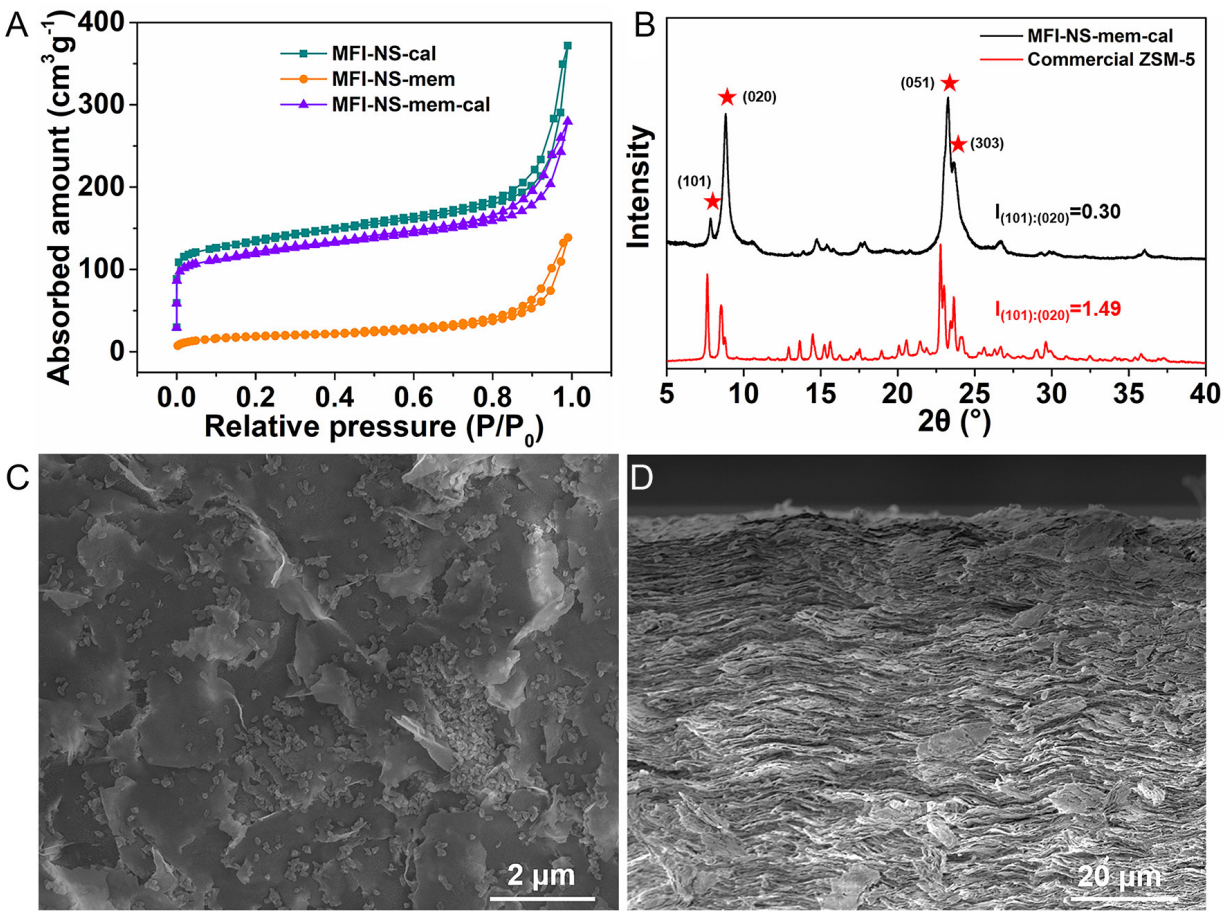

Figure 2. (A) N_2 adsorption-desorption isotherms of calcinated MFI-NS (MFI-NS-cal), MFI-NS membrane (MFI-NS-mem), and calcinated MFI-NS membrane (MFI-NS-mem-cal). (B) XRD patterns of MFI-NS-mem-cal and commercial ZSM-5. (C) Top-surface and (D) cross-section morphology of MFI-NS-mem-cal.

only larger interparticle voids exceeding 14 Å (MFI-NS-mem in Figure 2A and Supplementary Table 1), which impairs the otherwise homogeneous transportation of Zn^{2+}. Furthermore, while self-assembly renders the membrane structurally tailorable, it lacks sufficient mechanical strength to resist potential dendrite growth. Therefore, the membrane was calcined at 550 °C to remove the SDA and produce a self-supporting separator. Under 0.2 mm min^{-1} tension, the obtained MFI-NS separator is two orders of magnitude stronger than that of the GF separator [Supplementary Figure 4], which can offer remarkable mechanical robustness against dendrite penetration.

After calcination, the characteristic ~0.6 nm micropores of the MFI framework are restored [Figure 2A, Supplementary Table 1]. Concurrently, the weak low-angle peaks below 8° in the XRD pattern [Figure 1B] completely disappear [Figure 2B], confirming the removal of organic templates and the sintering of adjacent nanosheets. The sintering proceeds via the dehydration of adjacent Si-OH groups in the MFI-NS[55,56], as evidenced by the diminishing of the Si-OH peak in the FT-IR spectra [Supplementary Figure 5]. The calcined MFI-NS separator (MFI-NS-mem-cal in Figure 2A and Supplementary Table 1) exhibits a specific surface area of 383 m^2 g^{-1}, comparable to that of the calcined nanosheets (MFI-NS-cal in Figure 2A and Supplementary Table 1), indicating that calcination and concurrent sintering do not noticeably reduce the specific surface area. The restoration of micropores, together with the retention of high surface area, ensures efficient Zn^{2+} transport, as shown in later sections.

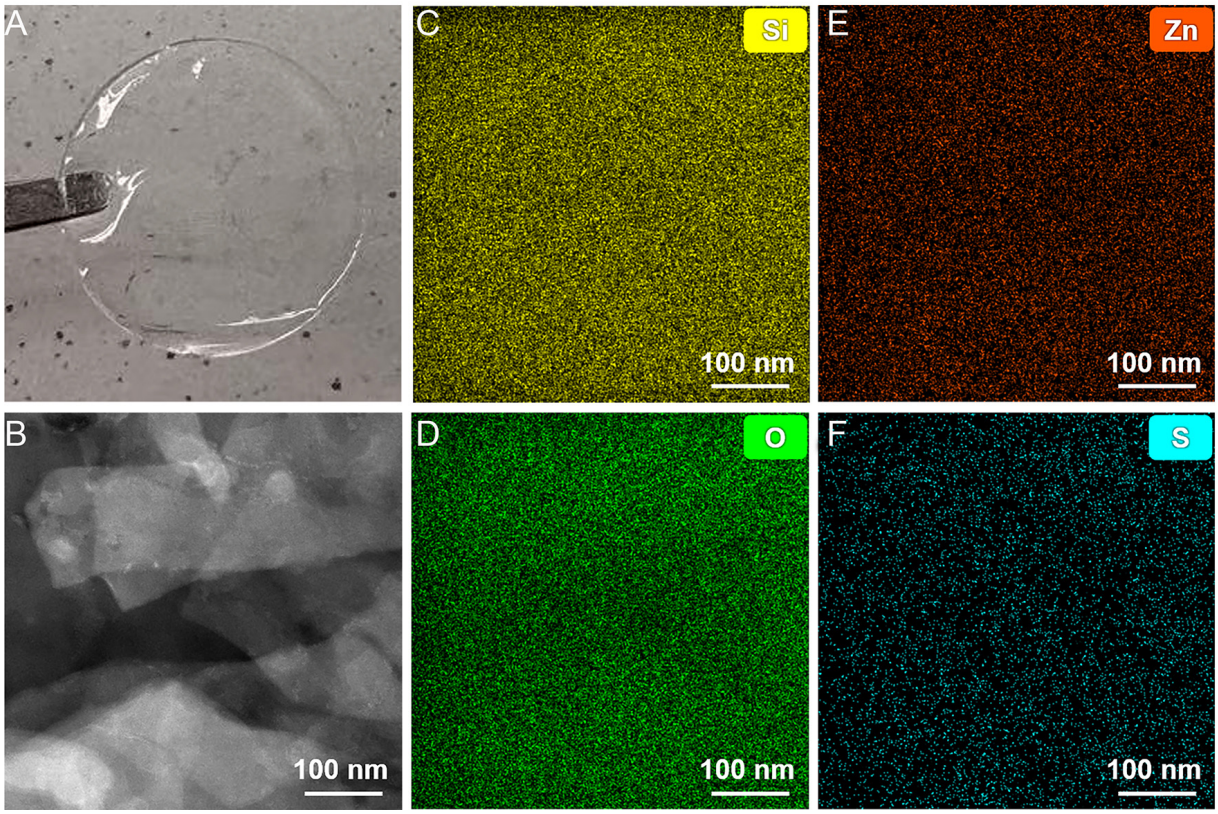

Figure 3. (A) Digital photograph showing the MFI-NS separator wet with electrolyte. (B) High-angle annular dark-field STEM morphology and (C-F) elemental distributions of a region in the MFI-NS separator. Digital photograph was taken by the authors.

Notably, the preferred [010]-orientation is further enhanced after calcination [Figure 2B]. The $I_{(101)}/I_{(020)}$ intensity ratio decreases from 0.60 to 0.30, which is substantially lower than that of commercial ZSM-5 (1.49)[57]. Consistently, the surface morphology exhibits well-aligned, face-on stacking of lamellar MFI-NS [Figure 2C and D]. The enhanced pore alignment is expected to further improve Zn^{2+} transport efficiency, approaching that of a single crystal oriented along the *b*-axis.

To be practically employed in AZIBs, the MFI-NS separator was wetted with the electrolyte, specifically a 3 M $ZnSO_4$ solution. The contact angle is 29°, indicating that the MFI-NS separator exhibits good wettability to the electrolyte [Supplementary Figure 6]. When 50 μL of the electrolyte was dropped onto the surface, the separator turned fully transparent, confirming sufficient electrolyte infiltration [Figure 3A]. The distribution of the electrolyte critically affects the electrochemical performance and was examined via high-angle annular dark-field scanning transmission electron microscopy (HAADF-STEM) combined with energy-dispersive X-ray spectroscopy elemental mapping. As demonstrated in Figure 3B-F, there are no obvious elemental segregations, suggesting that the electrolyte is homogeneously distributed.

Linear sweep voltammetry was performed to evaluate the corrosion of the Zn anode. As shown in Figure 4A, the anode paired with the MFI-NS separator exhibits a negligible hydrogen evolution reaction current compared to that paired with GF, indicating effective suppression of hydrogen evolution. The Tafel plot in Figure 4B further reveals that while the Zn anode with the MFI-NS separator displays a corrosion potential comparable to that with GF, its corrosion current (0.1160 mA) is an order of magnitude lower than that of GF (1.9331 mA). This substantial reduction suggests superior corrosion resistance enabled by the MFI-NS separator. Collectively, these results demonstrate that the MFI-NS separator effectively mitigates parasitic side reactions at the Zn anode, thereby likely extending the cycle life of AZIBs.

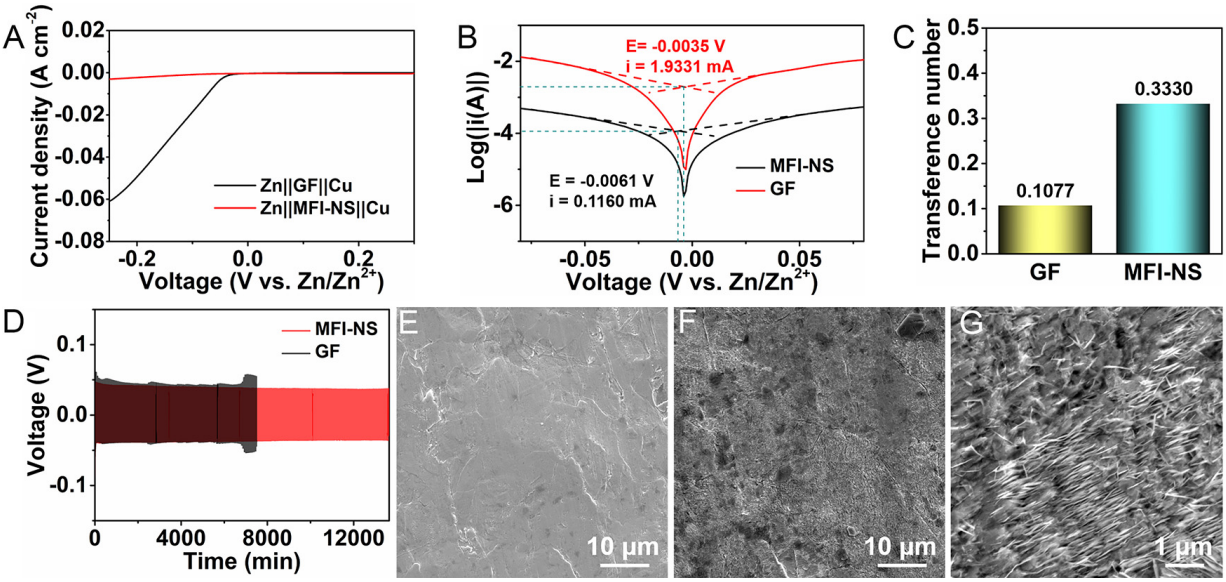

Figure 4. (A) Linear sweep voltammogram, (B) Tafel plots, (C) Zn^{2+} transference numbers for MFI-NS and GF separators. (D) Long-term cycling performance of symmetric cells at 1 mA cm^{-2} and 0.5 mAh cm^{-2}. (E-G) Surface morphology of Zn anodes after 200 h of cycling in symmetric cells with (E) MFI-NS and (F and G) GF separators.

In addition to side reactions, Zn^{2+} transport is a critical factor influencing the performance of AZIBs and was evaluated by EIS [Supplementary Figures 7 and 8]. The calculated Zn^{2+} transference number (t_{Zn}^{2+}) for the MFI-NS separator reaches 0.333, approximately three times that of the GF separator [Figure 4C]. The elevated t_{Zn}^{2+} reduces concentration polarization and enables more uniform ion transport, which could further suppress Zn dendrite formation[35]. Notably, the t_{Zn}^{2+} for MFI-NS separator is ~50% lower than that measured in MFI/polymer composites[35]. To exclude the effect of polymers and make a fair comparison between the separators with and without well-aligned straight channels, separators made by binder-free MFI granular particles (MFI-GP) were tested. The $I_{(101)}/I_{(020)}$ ratio in the XRD pattern of MFI-GP is 1.19 [Supplementary Figure 9], close to that for randomly dispersed MFI powder (1.49) and significantly larger than that for MFI-NS separators (0.30), confirming the absence of preferential channel alignment in the MFI-GP separator. The t_{Zn}^{2+} for the MFI-GP separator is 0.091, significantly lower than that of MFI-NS. In addition, from the impedance spectra in Supplementary Figure 10, the ionic conductivity for MFI-NS and MFI-GP is estimated to be 0.336 and 0.207 mS cm^{-1}, respectively. The remarkably higher t_{Zn}^{2+} and ionic conductivity for MFI-NS compared to MFI-GP suggest that the well-aligned straight channels in MFI-NS facilitate the transport of Zn ions.

To assess the efficacy of MFI-NS separators in suppressing dendrite formation on the Zn anode, long-term galvanostatic Zn plating/stripping cycling was performed using Zn||Zn symmetric cells. At a current density of 1 mA cm^{-2} and an areal capacity of 0.5 mAh cm^{-2}, the cell with the MFI-NS separator maintains stable cycling for over 12,000 min, whereas the cell with the GF separator shortcircuits after only approximately 7,500 min [Figure 4D]. When the areal capacity is increased to 1 mAh cm^{-2}, the MFI-NS cell sustains stable cycling for over 9,000 min, which is four times longer than the GF cell [Supplementary Figure 11].

The origin of the enhanced performance was further investigated by disassembling the symmetric cells after 12,000 min of cycling and examining the Zn electrode surfaces. The Zn electrode paired with the MFI-NS separator exhibits a significantly smoother surface than that paired with GF [Supplementary Figure 12]. Further SEM examinations reveal that the anode from the MFI-NS cell maintains a smooth and dense surface with no evidence of dendrite formation [Figure 4E]. In contrast, the anode from the GF cell displays

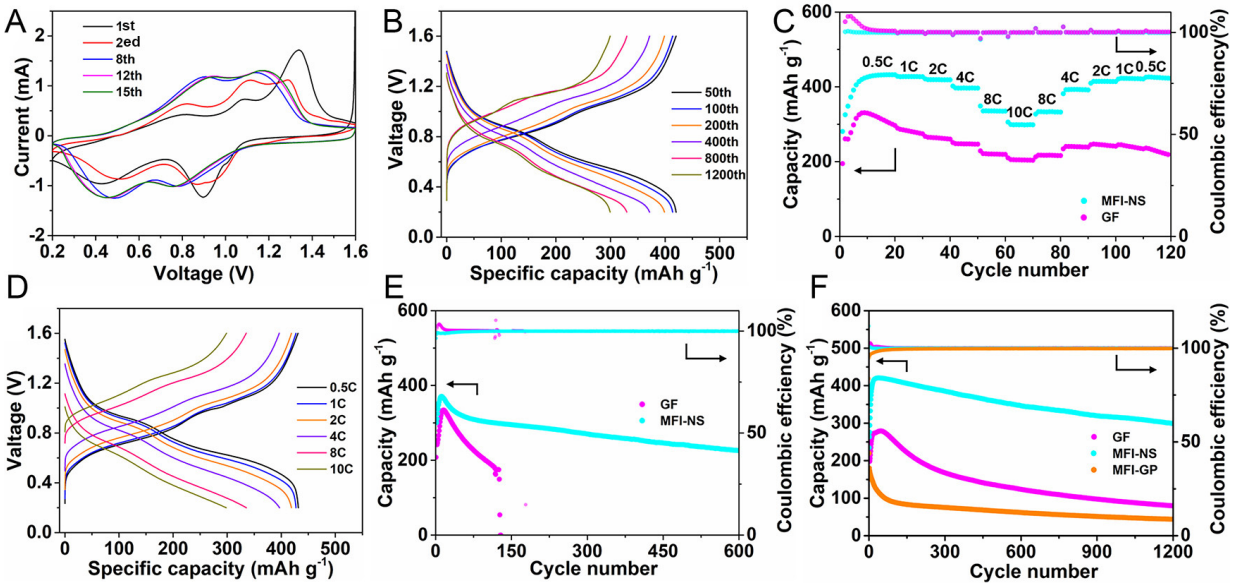

Figure 5. (A) CV of V_2O_5||MFI-NS||Zn cells. (B) Galvanostatic charge-discharge profiles at 1 A g^{-1}. (C) Rate performance of V_2O_5||MFI-NS||Zn and V_2O_5||GF||Zn cells. (D) Charge-discharge profiles at various current densities. (E and F) Long-term cycling at 0.5 A g^{-1} (E) and 1 A g^{-1} (F).

random zinc protrusions across the bare zinc foil, which is indicative of uncontrollable dendrite growth and undesirable side reactions [Figure 4F and G]. Collectively, these results demonstrate that the MFI-NS separator effectively regulates Zn deposition on the electrode surface, thereby enabling efficient suppression of dendrites.

Practical applicability of the MFI-NS separator was further assessed in full cells with V_2O_5 as the cathode and Zn foil as the anode. The CV curves [Figure 5A] exhibit multiple electrochemical redox peaks consistent with conventional V_2O_5||Zn systems[35,58,59]. Notably, in the first cycle, the CV curve exhibits three redox pairs. The dominant pair at 1.34/0.99 V is likely caused by trapped H_2O molecules acting as interlayer pillars that stabilize the structure during Zn^{2+} (de)intercalation[59]; this pair gradually diminishes in subsequent cycles. In contrast, the pairs at 0.82/0.43 and 1.08/0.90 V, corresponding to the stepwise intercalation and deintercalation of Zn^{2+} ions, are relatively weak in the first cycle, but become dominant and shift to 0.93/0.46 and 1.17/0.77 V after the first two cycles, respectively. Specifically, the redox pair at 0.93/0.46 V is attributed to the $V^{4+} \leftrightarrow V^{3+}$ transition, whereas the pair at 1.17/0.77 V corresponds to the $V^{5+} \leftrightarrow V^{4+}$ transition[60,61]. Consistently, galvanostatic charge-discharge profiles display two distinct pseudo-plateaus during both charging and discharging [Figure 5B], corresponding to the changes in vanadium valence state[35,61].

The V_2O_5||MFI-NS||Zn full cell exhibits outstanding rate performance compared with the GF-based counterpart [Figure 5C and D]. At current densities of 0.5C, 1C, 2C, 4C, 8C, and 10C (1C = 589 mA g^{-1}), the MFI-NS cell delivers specific capacities of 432, 427, 418, 396, 335, and 298 mAh g^{-1}, respectively [Figure 5C and D]. Upon returning to 0.5C from 10C, the capacity recovers to 426 mAh g^{-1}, corresponding to a recovery rate of 98.6%. Compared with previously reported composite separators consisting of MFI zeolites and polymer binders[35], the MFI-NS membrane demonstrates slightly superior rate capability and capacity retention [Supplementary Table 2]. Long-term cycling at 0.5 A g^{-1} [Figure 5E] and 1 A g^{-1} [Figure 5F] further confirms the high stability of V_2O_5||MFI-NS||Zn. Specifically, after 600 cycles at 0.5 A g^{-1}, the capacity retention remains at 61% (226 mAh g^{-1}), and after 1,200 cycles at 1 A g^{-1}, a retention of 71% (300 mAh g^{-1}) is achieved. The full cell also exhibits remarkable performance under both much lower (0.1 A g^{-1}) and higher (5 A g^{-1}) current densities [Supplementary Figure 13], demonstrating robust cycling across a wide range of

operating conditions. As V and S were detected on the Zn electrode after 400 cycles [Supplementary Figure 14], the performance degradation during long-term cycling is likely caused by cathode dissolution and anode passivation.

The exceptional electrochemical performance of V_2O_5||MFI-NS||Zn is attributed to the suppression of side reactions at the anode, enhanced Zn^{2+} transport, and inhibition of dendrite growth enabled by the uniform micropores of the MFI-NS separator. Expectedly, with the straight channels randomly oriented, the MFI-GP-based cell achieves only around 220 mAh g^{-1} initially and retains 44 mAh g^{-1} after 1,200 cycles [Figure 5F], which corroborates that the highly oriented straight channels are crucial for the superior electrochemical performance of the MFI-NS separators.

CONCLUSIONS

In this work, we have developed binder-free, highly [010]-oriented MFI-NS separators that simultaneously address multiple degradation mechanisms in AZIBs. The self-assembled lamellar separators are characterized by well-aligned straight channels perpendicular to the electrode surface, delivering a Zn^{2+} transference number 266% higher and an ionic conductivity 62% higher than those of separators comprising randomly oriented MFI particles, which thereby enables rapid and efficient Zn^{2+} transport. Concurrently, the uniform micropores in MFI zeolites promote homogeneous zinc deposition and regulate water transportation, effectively retarding dendrite formation and suppressing hydrogen evolution, respectively. The binder-free strategy further provides exceptional mechanical robustness, with tensile strength two orders of magnitude higher than that of commercial GF separators. These synergistic benefits endow MFI-NS separators with outstanding electrochemical performance. The V_2O_5||MFI-NS||Zn full cell delivers a specific capacity of 420 mAh g^{-1} at 1 A g^{-1} and retains 71% of its initial capacity after 1200 cycles, substantially outperforming the cells with separators comprising glass fibers or randomly oriented MFI particles.

DECLARATIONS

Authors' contribution

Data curation: Zhang, H. (Haoyu Zhang); Wen, X.; Xu, A.; Chen, S.
Collecting the literature: Zhang, H. (Haoyu Zhang); Lin, H.
Writing-original draft: Zhang, H. (Haoyu Zhang) Lin, H.; Wen, X.
Conceptualization, supervision, writing-review & editing, funding acquisition: Ma, L.; Han, Y.; Zhang, H. (Hui Zhang)

Availability of data and materials

The raw data supporting the findings of this study are available within this Article and its Supplementary Materials. Further data are available from the corresponding authors upon request.

AI and AI-assisted tools statement

Not applicable.

Financial support and sponsorship

This work was supported by the National Natural Science Foundation of China (No. 52473234, No. 92577112); Guangdong Innovative and Entrepreneurial Research Team Program (No. 2023ZT10C139); Guangzhou GJYC Program (No. 2024D03J0001).

Conflicts of interest

All authors declared that there are no conflicts of interest.

Ethical approval and consent to participate

Not applicable.

Consent for publication

Not applicable.

Supplementary Materials

Supplementary Materials

REFERENCES

1. Davis, S. J.; Lewis, N. S.; Shaner, M.; et al. Net-zero emissions energy systems. *Science* **2018**, *360*, eaas9793. DOI
2. Veers, P.; Dykes, K.; Lantz, E.; et al. Grand challenges in the science of wind energy. *Science* **2019**, *366*, eaau2027. DOI
3. Ji, X. A paradigm of storage batteries. *Energy. Environ. Sci.* **2019**, *12*, 3203-24. DOI
4. Ye, C.; Tu, S.; Zhang, S.; Wang, C.; Qiao, S. Harnessing interfacial solvation structure for next-generation secondary batteries. *Nat. Energy.* **2026**, *11*, 167-75. DOI
5. Jia, X.; Liu, C.; Neale, Z. G.; Yang, J.; Cao, G. Active materials for aqueous zinc ion batteries: synthesis, crystal structure, morphology, and electrochemistry. *Chem. Rev.* **2020**, *120*, 7795-866. DOI
6. Liu, Y.; Lu, X.; Lai, F.; et al. Rechargeable aqueous Zn-based energy storage devices. *Joule* **2021**, *5*, 2845-903. DOI
7. Tang, M.; Liu, Q.; Zou, X.; Zhang, B.; An, L. High-energy-density aqueous zinc-ion batteries: recent progress, design strategies, challenges, and perspectives. *Adv. Mater.* **2025**, *37*, 2501361. DOI PubMed PMC
8. Qin, Y.; Liu, P.; Zhang, Q.; et al. Advanced filter membrane separator for aqueous zinc-ion batteries. *Small* **2020**, *16*, 2003106. DOI
9. Li, Z.; Sha, W.; Xu, N.; Meng, L. Dual suppression of dendrite growth and hydrogen evolution reaction in aqueous Zn-ion batteries via selective binding of H^+ and Zn^{2+}. *Chem. Eng. J.* **2026**, *534*, 174974. DOI
10. Rana, A.; Faisal, M. A.; Nguyen, J. H.; et al. An electroanalytical perspective on the competitive interplay between zinc deposition and hydrogen evolution in aqueous zinc metal batteries. *Adv. Energy. Mater.* **2025**, *16*, e03630. DOI
11. Li, J.; Li, C.; Liu, B.; Li, Y.; Borodin, O.; Nazar, L. F. Aqueous eutectic electrolytes suppress oxygen and hydrogen evolution for long-life Zn||MnO_2 dual-electrode-free batteries. *Nat. Energy.* **2026**, *11*, 299-312. DOI
12. Yang, G.; Li, Q.; Ma, K.; Hong, C.; Wang, C. The degradation mechanism of vanadium oxide-based aqueous zinc-ion batteries. *J. Mater. Chem. A.* **2020**, *8*, 8084-95. DOI
13. Liu, R.; Hong, F.; Dai, Q.; et al. Insight into the corrosion microcell and passivation mechanisms of a Zn anode for aqueous zinc-ion batteries. *Energy. Environ. Sci.* **2025**, *18*, 5998-6008. DOI
14. Peng, H.; Ge, W.; Ma, X.; Jiang, X.; Zhang, K.; Yang, J. Surface engineering on zinc anode for aqueous zinc metal batteries. *ChemSusChem* **2024**, *17*, e202400076. DOI
15. Baek, M.; Kim, J.; Kim, M.; et al. Removing passivation irregularities for seamless electroplating across lithium, zinc, and magnesium metal batteries. *Chem* **2026**, *12*, 102879. DOI
16. He, H.; Qin, H.; Wu, J.; et al. Engineering interfacial layers to enable Zn metal anodes for aqueous zinc-ion batteries. *Energy. Storage. Mater.* **2021**, *43*, 317-36. DOI
17. Meng, H.; Ran, Q.; Dai, T. Y.; et al. Lamellar nanoporous metal/intermetallic compound heterostructure regulating dendrite-free zinc electrodeposition for wide-temperature aqueous zinc-ion battery. *Adv. Mater.* **2024**, *36*, 2403803. DOI
18. Zhu, Y.; Huang, Z.; Zheng, M.; et al. Scalable construction of multifunctional protection layer with low-cost water glass for robust and high-performance zinc anode. *Adv. Funct. Mater.* **2023**, *34*, 2306085. DOI
19. Li, L.; Yin, C.; Xiong, Y.; Zhong, G.; Hu, J. Cake-shaped $ZnMn_2O_4$ with enhancing pseudo-capacitance for efficient zinc storage. *J. Energy. Storage.* **2026**, *152*, 120798. DOI
20. Ding, C.; Zhao, Y.; Yin, W.; Kang, F.; Huang, W.; Zhang, Q. Regulating intermolecular hydrogen bonds in organic cathode materials to realize ultra-stable, flexible and low-temperature aqueous zinc-organic batteries. *Angew. Chem. Int. Ed.* **2024**, *64*, e202417988. DOI PubMed
21. Shi, Z.; Li, M.; Fu, X.; Zhang, Y.; Jiao, S.; Zhao, Y. Bimodal block molecule with ether-type and hydroxyl-type oxygen stabilizes Zn anode in super-dilute electrolyte. *Adv. Funct. Mater.* **2024**, *34*, 2316427. DOI
22. Li, J.; Guo, Z.; Wu, J.; et al. Dextran: a multifunctional and universal electrolyte additive for aqueous Zn ion batteries. *Adv. Energy. Mater.* **2023**, *13*, 2301743. DOI
23. He, L.; Lin, C.; Zeng, L.; et al. Synergistic regulation of anode and cathode interphases via an alum electrolyte additive for high-performance aqueous zinc-vanadium batteries. *Angew. Chem. Int. Ed.* **2024**, *64*, e202415221. DOI

24. Yang, S.; Zhang, Y.; Zhang, Y.; et al. Designing anti-swelling nanocellulose separators with stable and fast ion transport channels for efficient aqueous zinc-ion batteries. *Adv. Funct. Mater.* **2023**, *33*, 2304280. DOI
25. Qin, H.; Chen, W.; Kuang, W.; et al. A nature-inspired separator with water-confined and kinetics-boosted effects for sustainable and high-utilization Zn metal batteries. *Small* **2023**, *19*, 2300130. DOI
26. Wang, Q.; Zhao, J.; Zhang, J.; et al. Biomass chitin nanofiber separators proactively stabilizing zinc anodes for dendrite-free aqueous zinc-ion batteries. *Adv. Funct. Mater.* **2024**, *34*, 2405957. DOI
27. Zong, Y.; He, H.; Wang, Y.; et al. Functionalized separator strategies toward advanced aqueous zinc-ion batteries. *Adv. Energy. Mater.* **2023**, *13*, 2300403. DOI
28. Qin, Y.; Wang, X. Preventing dissolution of cathode active materials by ion-anchoring zeolite-based separators for durable aqueous zinc batteries. *Angew. Chem. Int. Ed.* **2023**, *63*, e202315464. DOI
29. Song, Y.; Ruan, P.; Mao, C.; et al. Metal-organic frameworks functionalized separators for robust aqueous zinc-ion batteries. *Nano. Micro. Lett.* **2022**, *14*, 218. DOI PubMed PMC
30. Lee, Y. H.; Jeoun, Y.; Kim, J. H.; et al. Selective ion transport layer for stable aqueous zinc-ion batteries. *Adv. Funct. Mater.* **2023**, *34*, 2310884. DOI
31. Xu, J.; Yang, Y.; Dai, Q.; et al. Towards ultra-stable wide-temperature zinc-ion batteries by using ion-sieving organic framework membrane. *Angew. Chem. Int. Ed.* **2025**, *64*, e202423118. DOI
32. Yuan, Z.; Zhu, X.; Li, M.; Lu, W.; Li, X.; Zhang, H. A highly ion-selective zeolite flake layer on porous membranes for flow battery applications. *Angew. Chem. Int. Ed.* **2016**, *55*, 3058-62. DOI
33. Cui, Y.; Zhao, Q.; Wu, X.; et al. An interface-bridged organic-inorganic layer that suppresses dendrite formation and side reactions for ultra-long-life aqueous zinc metal anodes. *Angew. Chem. Int. Ed.* **2020**, *59*, 16594-601. DOI
34. Chang, Z.; Qiao, Y.; Yang, H.; et al. Sustainable lithium-metal battery achieved by a safe electrolyte based on recyclable and low-cost molecular sieve. *Angew. Chem. Int. Ed.* **2021**, *60*, 15572-81. DOI
35. Zhu, J.; Bie, Z.; Cai, X.; et al. A molecular-sieve electrolyte membrane enables separator-free zinc batteries with ultralong cycle life. *Adv. Mater.* **2022**, *34*, 2207209. DOI
36. Li, Z.; Wu, X.; Yu, X.; et al. Long-life aqueous Zn-I_2 battery enabled by a low-cost multifunctional zeolite membrane separator. *Nano. Lett.* **2022**, *22*, 2538-46. DOI
37. Yang, H.; Qiao, Y.; Chang, Z.; et al. Reducing water activity by zeolite molecular sieve membrane for long-life rechargeable zinc battery. *Adv. Mater.* **2021**, *33*, 2102415. DOI
38. Li, Z.; Zhou, S.; Wu, X.; et al. Restraining shuttle effect in rechargeable batteries by multifunctional zeolite coated separator. *Adv. Funct. Mater.* **2022**, *33*, 2211774. DOI
39. Zhang, D.; Huang, K.; Xia, Y.; et al. Two-dimensional MFI-type zeolite flow battery membranes. *Angew. Chem. Int. Ed.* **2023**, *62*, e202310945. DOI
40. Xia, Y.; Cao, H.; Xu, F.; et al. Polymeric membranes with aligned zeolite nanosheets for sustainable energy storage. *Nat. Sustain.* **2022**, *5*, 1080-91. DOI
41. Shang, W.; Li, Q.; Jiang, F.; et al. Boosting Zn||I_2 battery's performance by coating a zeolite-based cation-exchange protecting layer. *Nano. Micro. Lett.* **2022**, *14*, 82. DOI PubMed PMC
42. Wang, D.; Chang, L.; Xie, Y.; et al. Zeolite-filled glass fiber separator enables Ah-level zinc ion batteries via synergistic dual-electrodes regulation. *ACS. Nano.* **2026**, *20*, 4279-90. DOI
43. Zhang, J.; Zhou, A.; Gawande, K.; et al. *b*-axis-oriented ZSM-5 nanosheets for efficient alkylation of benzene with methanol: synergy of acid sites and diffusion. *ACS. Catal.* **2023**, *13*, 3794-805. DOI
44. Jeon, M. Y.; Kim, D.; Kumar, P.; et al. Ultra-selective high-flux membranes from directly synthesized zeolite nanosheets. *Nature* **2017**, *543*, 690-4. DOI
45. Varoon, Agrawal. K.; Zhang, X.; Elyassi, B.; et al. Dispersible exfoliated zeolite nanosheets and their application as a selective membrane. *Science* **2011**, *334*, 72-5. DOI
46. Kim, D.; Jeon, M. Y.; Stottrup, B. L.; Tsapatsis, M. *para*-Xylene ultra-selective zeolite MFI membranes fabricated from nanosheet monolayers at the air-water interface. *Angew. Chem. Int. Ed.* **2017**, *57*, 480-5. DOI PubMed
47. Kim, D.; Ghosh, S.; Akter, N.; et al. Twin-free, directly synthesized MFI nanosheets with improved thickness uniformity and their use in membrane fabrication. *Sci. Adv.* **2022**, *8*, eabm8162. DOI PubMed PMC
48. Min, B.; Yang, S.; Korde, A.; Kwon, Y. H.; Jones, C. W.; Nair, S. Continuous zeolite MFI membranes fabricated from 2D MFI nanosheets on ceramic hollow fibers. *Angew. Chem. Int. Ed.* **2019**, *58*, 8201-5. DOI PubMed
49. Duan, X.; Kim, D.; Narasimharao, K.; Al-Thabaiti, S.; Tsapatsis, M. High-performance ammonia-selective MFI nanosheet membranes. *Chem. Commun.* **2021**, *57*, 580-2. DOI PubMed

50. Xia, Y.; Hou, X.; Chen, X.; et al. Membrane with horizontally rigid zeolite nanosheet arrays against zinc dendrites in zinc-based flow battery. *Chem. Eng. J.* **2023**, *465*, 142912. DOI
51. Iskhakova, L.; Cao, Z.; Sun, X.; Gabski, J.; Dong, J. Preactivated zeolite nanosheet plate-tiled membrane on porous PVDF film: synthesis and study of proton-selective ion conduction. *J. Membr. Sci.* **2023**, *669*, 121328. DOI
52. Zhai, Y.; Wu, Y.; Sheng, J.; et al. An open-pore MFI zeolite nanosheet-modified separator with Li-ion flux regulation for lithium-metal batteries. *Chem. Commun.* **2024**, *60*, 324-7. DOI
53. Yu, Y.; Yang, F.; Chen, X.; et al. MFI zeolite nanosheet composite membranes with both high lithium ion transport and sulfur fixation for lithium-sulfur batteries. *Ind. Eng. Chem. Res.* **2025**, *64*, 8425-32. DOI
54. Zhang, H.; Xiao, Q.; Guo, X.; et al. Open-pore two-dimensional MFI zeolite nanosheets for the fabrication of hydrocarbon-isomer-selective membranes on porous polymer supports. *Angew. Chem. Int. Ed.* **2016**, *55*, 7184-7. DOI
55. Gao, B.; Qiu, B.; Zheng, M.; et al. Dynamic self-dispersion of aggregated boron clusters into stable oligomeric boron species on MFI zeolite nanosheets under oxidative dehydrogenation of propane. *ACS. Catal.* **2022**, *12*, 7368-76. DOI
56. Walsh, G.; Hamilton, S. Adsorption of 2,4,6-trinitrotoluene on MFI zeolite. *Propellants. Explos. Pyrotech.* **2011**, *36*, 182-6. DOI
57. Lai, Z.; Tsapatsis, M.; Nicolich, J. Siliceous ZSM-5 membranes by secondary growth of *b*-oriented seed layers. *Adv. Funct. Mater.* **2004**, *14*, 716-29. DOI
58. Zhou, J.; Shan, L.; Wu, Z.; Guo, X.; Fang, G.; Liang, S. Investigation of V_2O_5 as a low-cost rechargeable aqueous zinc ion battery cathode. *Chem. Commun.* **2018**, *54*, 4457-60. DOI
59. Li, R.; Zhang, H.; Zheng, Q.; Li, X. Porous V_2O_5 yolk-shell microspheres for zinc ion battery cathodes: activation responsible for enhanced capacity and rate performance. *J. Mater. Chem. A.* **2020**, *8*, 5186-93. DOI
60. Wang, T.; Li, S.; Weng, X.; et al. Ultrafast 3D hybrid-ion transport in porous V_2O_5 cathodes for superior-rate rechargeable aqueous zinc batteries. *Adv. Energy. Mater.* **2023**, *13*, 2204358. DOI
61. Chen, D.; Lu, M.; Wang, B.; et al. High-mass loading $V_3O_7{\cdot}H_2O$ nanoarray for Zn-ion battery: new synthesis and two-stage ion intercalation chemistry. *Nano. Energy.* **2021**, *83*, 105835. DOI